Welding in the World
https://doi.org/10.1007/s40194-025-02213-0

RESEARCH PAPER

Microstructure and mechanical properties of laser welded PBF-LB/IN718

Saeid Parchegani Chozaki[1] · Heidi Piili[1] · Olli Nyrhila[2] · Antti Salminen[1]

Received: 30 May 2025 / Accepted: 13 October 2025

Abstract
Applications for additively manufactured (AM) metal parts, particularly via laser-based powder bed fusion (PBF-LB/M), have been growing significantly in industries with high level of requirements such as aerospace, nuclear plant, automotive, energy, and medical industry. However, PBF-LB/M parts often require welding to other components due to their limited size. Thus, the weldability of PBF-LB/M parts is of interest, particularly due to the microstructural differences between PBF-LB/M and conventionally manufactured parts. This study investigates the microstructure and mechanical properties of laser-welded PBF-LB/IN718 and compares the results with laser-welded sheet metal IN718. In addition, the effect of heat treatment before welding on the weldability of PBF-LB/IN718 samples was evaluated. Both the heat-treated and as-built PBF-LB/IN718 welds had lower microhardness at the fusion zone (FZ) than the base metals, whereas the sheet metal IN718 weld showed higher microhardness at FZ than the base metal. This was attributed to the distinct secondary phases and microstructure of the conventional IN718 and PBF-LB/IN718 samples. Nevertheless, the ultimate tensile strength and yield strength of PBF-LB/IN718 welds were higher than the conventional IN718 welds, proving that laser welding is a viable method of joining PBF-LB/IN718 parts. Finally, the fatigue strength of the PBF-LB/IN718 welds, assessed at 10^6 cycles, was inferior to that of the conventional IN718 welds, owning to the defects such as lack of fusion in the base metal of PBF-LB/IN718 samples.

Keywords Laser welding · Additive manufacturing · Powder bed fusion · IN718 · Tensile and fatigue test

1 Introduction

Additively manufactured parts are expanding their applications in different industrial sectors due to the advantage of design freedom which enables industries to customize and incorporate new features into their components, which is otherwise impossible to manufacture using conventional methods [1]. This could result in lower post-processing and machining costs. One good example of such material that has benefited from AM is Alloy 718. The alloy is the most used superalloy worldwide, covering more than half of superalloy usage due to its unique characteristics [2]. Alloy 718 is characterized as a high-strength, high-hardness, corrosion, and oxide resistant alloy for high-temperature applications up to 750 °C. However, the alloy is challenging to machine due to its high hardness; thus, using traditional subtractive machining leads to both tool wear and unavoidably time -consuming and expensive machining [3]. Therefore, industries are interested in the possibility of manufacturing this alloy via AM due to its extensive applications in a variety of industries [4]. PBF-LB is one the most utilized AM method for alloy 718 due to its geometry accuracy and high-density material production [5]. However, issues such as cracking, high residual stress, porosity, and lack of fusion are commonly reported in PBF-LB parts [6]. This means that the quality of the final parts is highly depended on the process parameters used in this process. Thus, its necessary to investigate the impact of process parameter on defects such as porosity and lack of fusion since these defects directly impact the mechanical properties of the parts [7].

Another aspect of the parts made by PBF-LB are limited in size due to the size of the building chamber of the machines [8]. Therefore, fusion welding is required to join

Recommended for publication by Commission IV - Power Beam Processes.

✉ Saeid Parchegani Chozaki
saeid.parcheganichozaki@utu.fi

[1] Department of Mechanical and Materials Engineering, University of Turku (UTU), Turku, Finland

[2] EOS Finland Oy, Turku, Finland

Published online: 12 November 2025

PBF-LB parts to other components in order to integrate PBF-LB parts into larger assemblies. This raises interest in their weldability since the microstructure of PBF-LB components differs from that of the wrought or cast material [9]. There has been extensive research on weldability of wrought or cast IN718 [10, 11]. Alloy 718 is generally considered as a weldable material due to its resistance to strain age cracking. However, hot liquation or microfissuring in heat affected zone (HAZ) is reported to be a major concern regarding the weldability of the alloy [12]. Another concern is the segregation of Nb in the weld, which results in precipitation of brittle Laves phases that deteriorate the mechanical properties of the weld [13]. Gas tungsten arc welding (GTAW) is the most used welding technique employed for joining Alloy 718 [14, 15]. However, high heat input of GTAW results in larger HAZ which in turn intensifies the microfissuring cracking. Therefore, laser beam and electron beam welding are proposed for joining the alloy as they provide lower heat input and narrower HAZ, consequently [16]. Nevertheless, some issues related to porosity and precipitation of brittle Laves and MC carbides phases are reported in laser welding of Alloy 718 [17]. Hence, it is of great importance to investigate the weldability of PBF-LB/IN718 compared to cast or wrought IN718 to understand to what degree our knowledge regarding the weldability of conventional IN718 is transferable to PBF-LB/IN718 components. In this regard, Jokish et al. [18] studied the laser welding of PBF-LB/IN718 and PBF-LB/IN625 tubes and stated that laser welding is a feasible way of joining these AM parts; however, the quality of the weld is severely impacted by the porosity. In another study, Simón-Muzás et al. [19] demonstrated that tensile strength of welded PBF-LB/IN718 are comparable with the cast IN718 base metal but less than that of the wrought base metal. They concluded that heat treatment and build orientation of PBF-LB/IN718 samples play a significant role in their tensile properties. In the same study, the impact of heat treatment was also investigated, and it was indicated that stress relieving followed by solution annealing results in joints with higher ductility than the double-aged heat-treated joints. No clear trend was observed between the build orientation and tensile properties in the study, however, the PBF-LB/IN718 samples printed at 45° (sample orientation with regard to the build platform) and welded to the wrought IN718 resulted in the lowest ultimate tensile strength and elongation. Solidification cracking or microcracking at the FZ of the PBF-LB/IN718 welds is also reported in some studies [15, 17]. The studies are very limited in this area and to the best knowledge of the author there has been a few studies published [8, 18, 19]. Therefore, more research is required to understand the relationship between the microstructure of PBF-LB/IN718 and their weldability particularly using laser welding.

The purpose of this work is to investigate the mechanical properties of PBF-LB/IN718 welds in regard to their microstructure evolution during laser welding. Microhardness, tensile, and fatigue tests are examined for the welds to assessed the strength and integrity of the welds. Wrought IN718 is used as a reference material in both as-weld and base metal conditions to compare the mechanical properties of the PBF-LB/IN718 welds. Additionally, the PBF-LB/IN718 samples are prepared in as-build (without heat treatment) and heat treated (solution annealing followed by double aging) to investigate the effect of pre-weld heat treatment on the mechanical properties and microstructure of the PBF-LB/IN718 welds. Thus, this study answers the question of how much of what we know about the welding of traditional wrought IN718 can be applied to the weldability of PBF-LB/IN718 parts, thus provides insight into the viability of integrating PBF-LB/IN718 parts into larger assemblies using laser welding.

2 Materials and methods

2.1 Materials

The PBF-LB/IN718 samples were manufactured by EOS Finland Oy using an EOS M290 machine equipped with a 400 W single mode fiber laser and a building volume of $250 \times 250 \times 325$ mm^3. The samples were manufactured horizontally with a dimension of $150 \times 50 \times 3.2$ mm as illustrated in Fig. 1. The printing parameters were set at hatch distance of 0.11 mm, scanning speed of 930 mm/s, layer thickness of 80 µm, and laser power of 350 W. The building platform

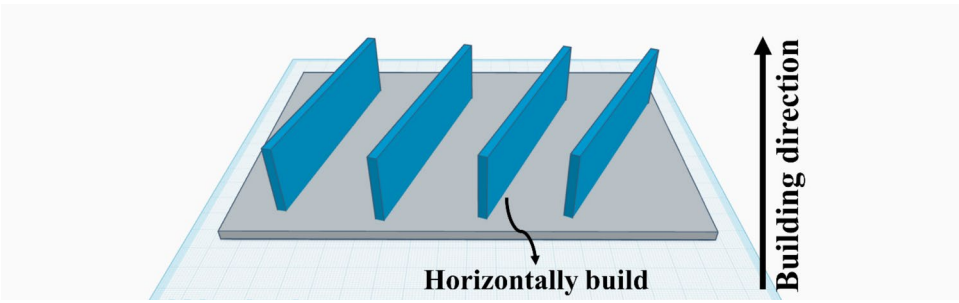

Fig. 1 Schematic of horizontally printed PBF-LB/IN718 in respect to the building direction

Table 1 Chemical composition of Alloy 718 in powder and wrought condition

Element	Fe	Ni	Cr	Mo	Nb	Ti	Al	C	B	Si
Alloy 718 powder	Bal	50.14	19.04	2.80	4.92	1.08	0.33	0.08	0.006	0.03
Alloy 718 wrought	18.03	53.49	18.23	3.00	5.17	1.04	0.46	0.03	0.002	0.07

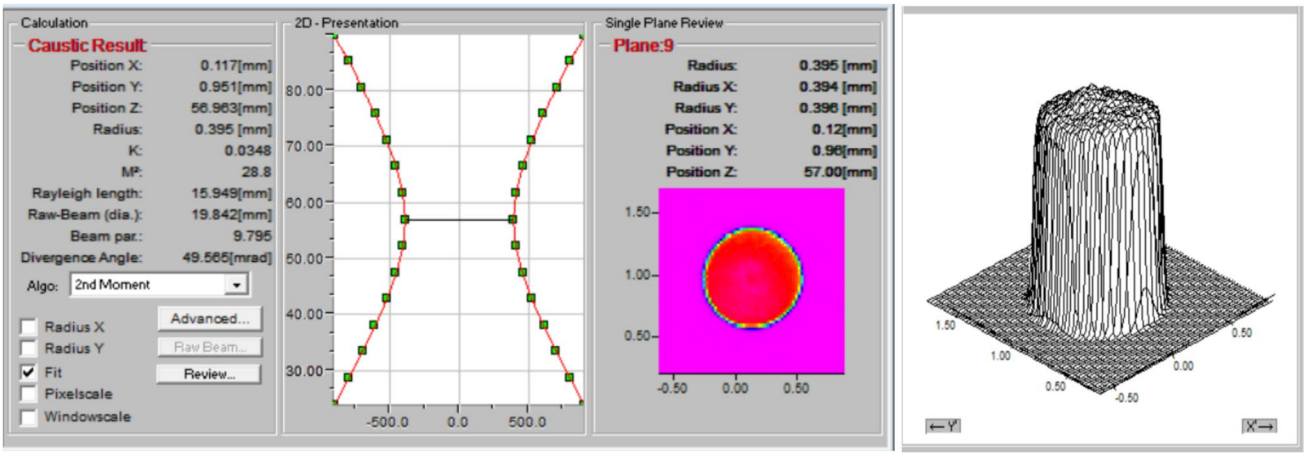

Fig. 2 Laser beam profile at the focal point

was preheated to 80 °C to minimize thermal stress between the components and the building platform, and it was maintained under controlled Ar gas to prevent oxidation during the process.

The samples were divided into two groups: the first group were welded in as-built condition (no heat treatment), while the second group underwent solution treatment (954 °C/1 h + air cooling) followed by double aging (718 °C/8 h + furnace cooling + 621 °C/18 h + air cool) before welding. The heat treatment process was carried out at EOS Finland Oy using an Ar gas furnace to prevent surface oxidation. The sheet metal samples of Alloy 718 were provided by HARLD PIHL AB (Sweden) in cold-rolled and annealed condition (ASTM B670-07). The wrought Alloy 718 samples were cut using laser with N_2 cutting gas and machined to the dimension of 150 × 50 × 3.2 mm. The chemical composition of each materials was provided by their manufacturers and are listed in Table 1. The edge of the samples, used as the joint edge, was machined and cleaned using acetone before welding.

2.2 Laser welding

Laser welding experiments were carried out utilizing an IPG YLS-10000S fiber laser with a maximum average power output of 10 kW and wavelength of 1070 nm. The laser beam was delivered to a welding head using an optical fiber with 300-µm diameter. The welding head included a 250-mm collimation module with a 400 -mm focal lens. The setup

Table 2 Laser welding parameters

Laser power (kW)	Welding speed (m/min)	Linear energy input (J/mm)	Focal point position (mm)	Gas flow rate (L/min)
3.0	3.0	75	− 2	20

provided a top-hat beam shape at the focal point with about 800 µm focal point diameter as shown in Fig. 2. A coaxial shielding gas nozzle was attached to the welding head to protect the weld pool from oxidation using Ar gas. The offset distance of the shielding gas nozzle was set at 5 mm from the workpiece and the Ar gas was fed to the nozzle with a flow rate of about 20 L/min. The welding parameters are listed in Table 2, and were optimized based on previous studies to achieve a fully penetrated weld according to ISO 13919–1 standard [17].

The base metal of specimens and the welds are labeled according to Table 3 for ease of reference to each specimen in the following sections.

2.3 Materials characterization

The welds cross-section was cut and ground using 200–800 grits SiC papers. The ground samples were polished with diamond suspensions and then electro-etched using 10% oxalic acid for about 10 s. The welds micrographs were imaged using a Wild M400 optical microscope, and the

Table 3 Acronyms used for the base metal and welded specimens

Acronyms	Definition
BMAB	The base metal of as-built (AB) PBF-LB/IN718
BMHT	The base metal of heat-treated (HT) PBF-LB/IN718
BM	The base metal of wrought Alloy 718
ABW	The as-built (AB) PBF-LB/IN718 in welded condition
HTW	The heat-treated (HT) PBF-LB/IN718 in welded condition
WW	The wrought Alloy 718 in welded condition

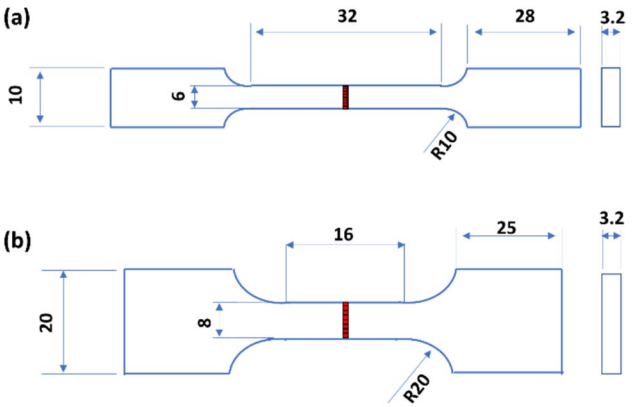

Fig. 3 The dimension of **a** tensile specimen, **b** fatigue specimen (dimension in mm)

microstructures were examined using a Thermo Scientific Apreo S electron scanning microscope equipped with Oxford instrument energy dispersive spectrometry (EDS). The phase identification in the base metals and FZs were carried out using an Empyrean X-ray diffractometer (with a Cu target). The X-ray beam size was reduced to width of 1 mm using 2 mm mask and a 1/16° divergence slit in order to collect data from the narrow area of the FZs. The X-ray data was refined utilizing Rietveld method and compered with the standard patterns obtained from Inorganic Crystal Structure database (ICSD). The Vickers microhardness was measured using a Struers DuraScan 70 in accordance with EN ISO 6507 standards. The applied load was 3 kgf, with a holding duration of 15 s.

The tensile tests were performed at room temperature utilizing a ZwickRoell tensile machine with a specified force capacity of 100 kN and displacement rate of 0.025 mm/s. For each weld, three tensile samples were evaluated, and the average results for ultimate tensile stress (UTS), 0.2% offset yield stress, and elongation were reported. Tensile test specimens were prepared according to ASTM E-8 standard as shown in Fig. 3a.

The fatigue tests were carried out using a servo hydraulic machine with stress ratio of R = 0.1 and frequency of about 90 Hz. Three specimen per weld were used to evaluate the fatigue strength at $N = 10^6$ cycles using the method described by Maxwell et al. [20]. The method considers the damage accumulated during each loading steps (loading steps of 20 MPa was used in this study) and fatigue strength (equivalent fully reversed stress amplitude considering R = 0.1) for each weld at 10^6 cycles was estimated using the following equations [21]:

$$\sigma = AN^{-1/b} \tag{1}$$

$$D = \sum_{i=1}^{l} D_i = \sum_{i=1}^{l} \frac{n_i}{N_i} \leq 1 \tag{2}$$

$$\mathrm{D} = \sum\nolimits_{i=1}^{l} n_i \left(\frac{\sigma_i}{A}\right)^b \leq 1 \tag{3}$$

where A and b are material parameters, D acumulated damage which equals 1 when the sample breaks, n_i number of cycles for each step, and σ_i stress amplitude at each step. It should be noted that all the stress amplitude was converted to fully reversed stress amplitude using Gerber criteria before applying the Basquin equation (Eq. (1)). The fatigue test samples for PBF-LB/IN718 were polished after welding to eliminate the effect of surface roughness on the fatigue results. The fatigue test specimens were prepared according to ISO 1099 standard as displayed in Fig. 3b.

3 Results and discussion

3.1 Weld cross-section geometry

The cross-section macrograph images of the welds are shown in Fig. 4. A full penetration weld and free from solidification cracking can be seen in all the welds, indicating that laser welding is a viable way of joining PBF-LB/IN718 parts. The weld zone area of the ABW and HTW is, on average, 10% larger than that of the WW. This could be due to differences in the surface roughness of the samples. The PBF process generally results in a rough surface finish due to the fast cooling and heating rate. As a result, PBF-LB/IN718 samples may have higher laser beam absorptivity than wrought Alloy 718. This agrees with the reports of other studies [22, 23]. Another factor that could impact the size of the weld zone area could be the differences in thermophysical properties, such as thermal conductivity of the PBF-LB/IN718 samples compared to wrought. However, this needs further investigation. The weld bead profiles on the top and root sides are provided in Fig. 5. It can be seen that all the welds display excessive penetration on the root side of about 250–350 µm.

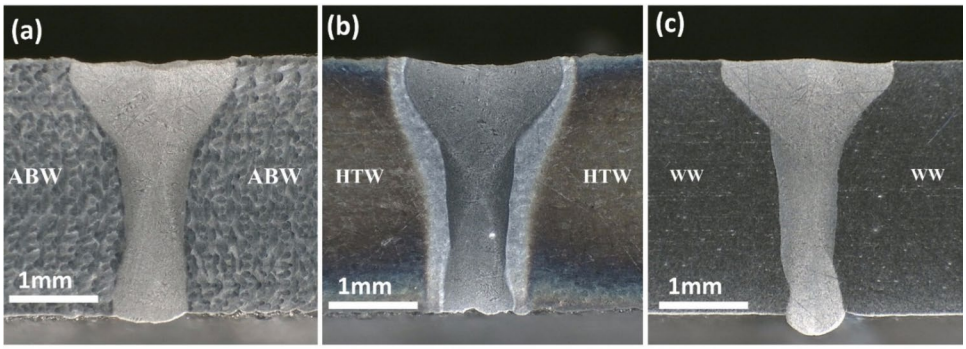

Fig. 4 Macrograph images of the cross-section of **a** ABW, **b** HTW weld, **c** and WW weld

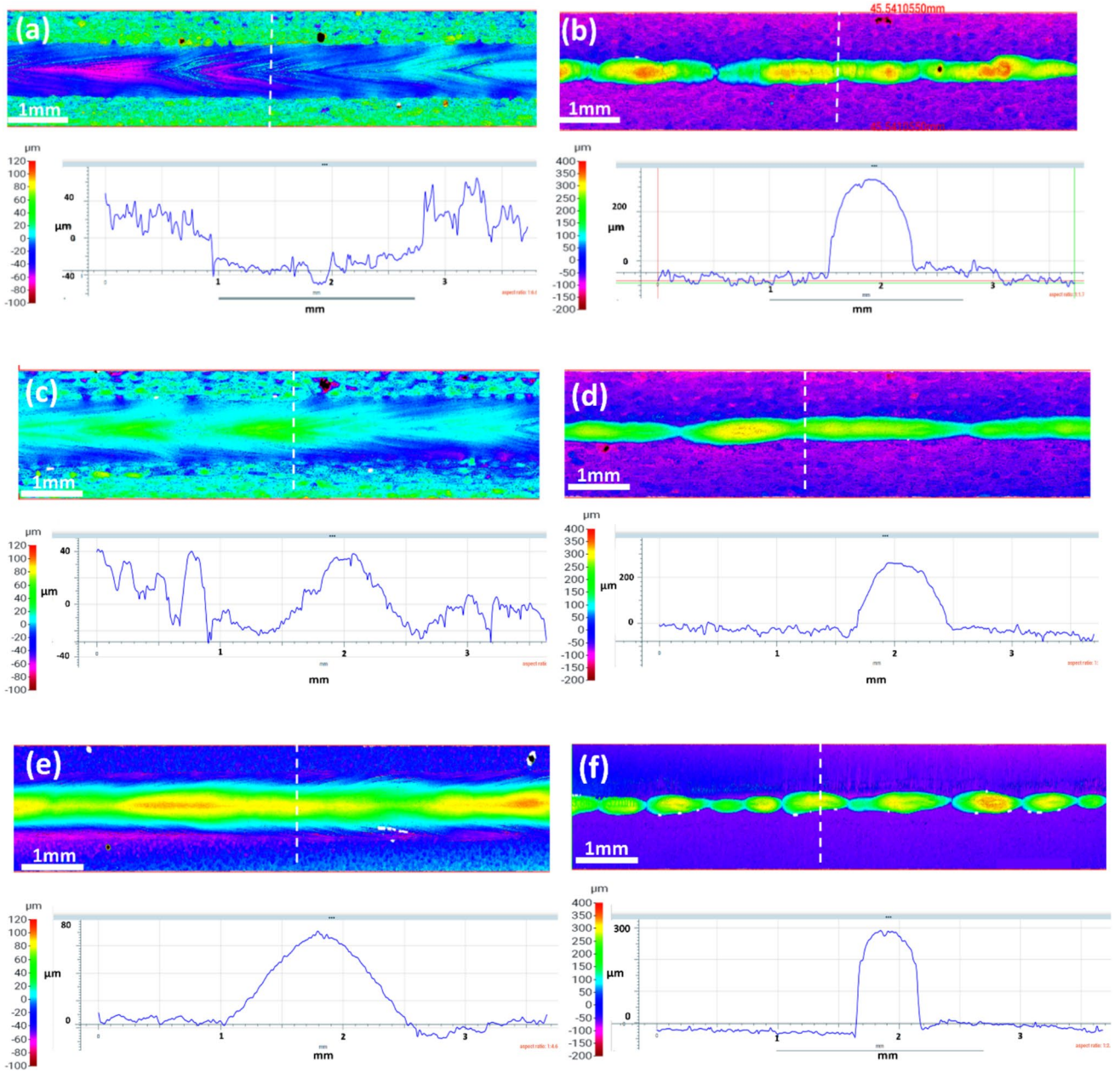

Fig. 5 The weld bead profile of **a** ABW top side, **b** ABW root side, **c** HTW top side, **d** HTW root side, **e** WW top side, **f** WW root side

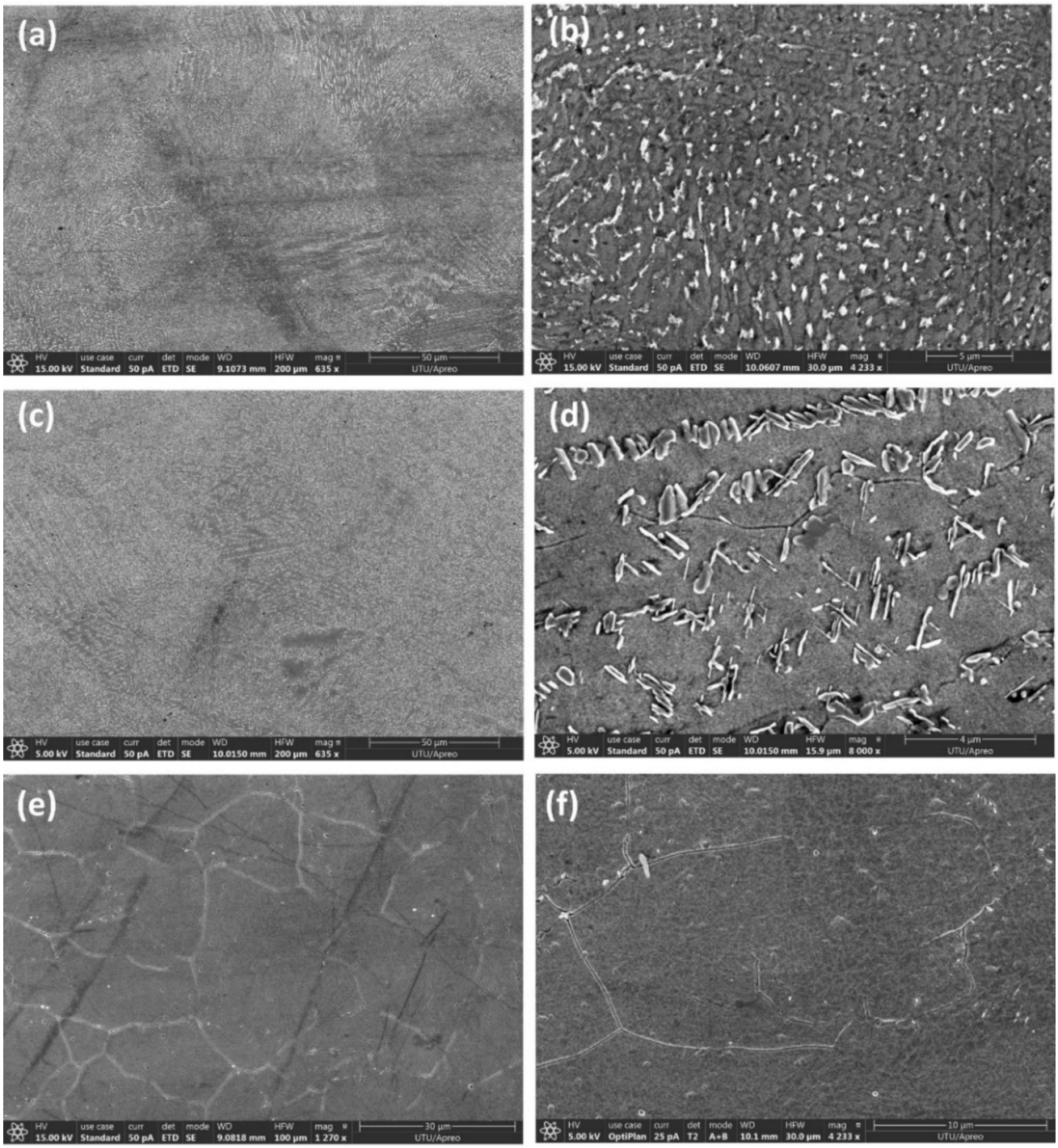

Fig. 6 Microstructure images of base metals of **a** BMAB sample, **c** HTBM sample, **e** BM sample. **b**, **d**, and **f** are the magnified images of **a**, **c**, and **e** respectively

The top side profile of the welds is, however, different based on their base metals. The ABW (Fig. 5a) shows underfill of about 20–40 µm, whereas the HTW (Fig. 5c) shows slight undercut of about 20–40 µm. The WW shows a very smooth weld surface on the top side with excess weld metal of about 80 µm (Fig. 5e). The differences in the weld surface geometry could impact the mechanical properties of the joints, particularly fatigue strength. Nevertheless, according to ISO 13919-1 standard, all three welds meet the requirements for the highest weld quality (level B), thus are considered for further mechanical and microstructural analysis in the following sections.

3.2 Microstructure characterization

3.2.1 Microstructure of the base metals

The microstructure of the base metals in all three conditions is shown in Fig. 6. Both BMHT and BMAB display a very fine dendritic microstructure (Fig. 6a and c), which is due to the fast heating and cooling involved in the PBF-LB process. The microstructure of the BMAB and BMHT is somewhat similar, indicating that the heat treatment at 954 °C did not result in recrystallization or homogenization of the microstructure of the BMAB. However, microstructure images at higher magnification reveal a distinct secondary phase that are precipitated at both grains and sub-grain regions, as shown in Fig. 6b and d. The BMAB displays somewhat interconnected secondary phases that are distributed all over the matrix. These phases are reported to be Laves and metallic carbide (MC), primarily NbC (niobium carbide), based on TEM analyses in other similar studies [24], whereas the BMHT reveals a very fine needle shape secondary phase precipitated in the microstructure following the heat treatment. The needle-shaped particles are reported to be delta phases that are precipitated into the matrix as a result of Laves phases dissolution following the heat treatment [24]. Dissolution of Laves phases releases more Nb into the matrix, which could then precipitate into the matrix as strengthening phases of γ' and γ'' following the two-step aging heat treatment. However, it seems that some of the released Nb is consumed by the Delta phase, which prevents further strengthening of the matrix. In contrast, the BM exhibits an equiaxed grain structure along with some minor secondary phases, as shown in Fig. 6e and f. The annealed solution heat treatment on the wrought Alloy 718 seems to be resulted in a homogenized microstructure, however, some minor secondary phases remain in the matrix, primarily at the grain boundaries, as illustrated in Fig. 6f. These secondary phases are known to be MC carbides that dissolve at higher temperatures and have been documented in previous related research [24, 25].

The XRD profile confirms the presence of the secondary phases in the base metals as shown in Fig. 7. It can be seen that the BMAB clearly shows diffraction peaks for Laves phases as expected (Fig. 7a). However, no MC carbide phases are detected by the XRD profile. This could be due to the low volume fraction of the MC carbide phases in the matrix. As for the BMHT, it can be seen that the Laves phase are dissolved and diffraction peaks related to Delta and MC carbides phases are detected in the XRD measurements (Fig. 7b). The XRD data does not confirm any diffraction peaks related to secondary phases for the BM (Fig. 7c), despite the microstructure image (Fig. 6f) showing the presence of MC carbides phases. This again could

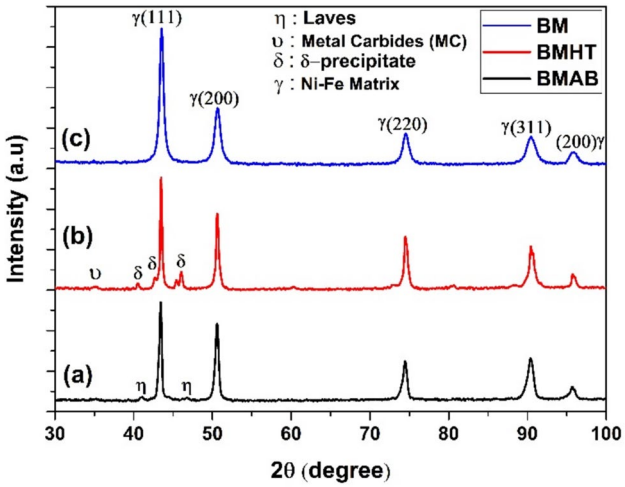

Fig. 7 XRD profile of base metals of **a** ABBM, **b** HTBM, **c** BM

be due to the low volume fraction of the MC carbide phases that are below the detection limit of the XRD measurement. It is worth mentioning that the diffraction peaks of γ' and γ'' overlap with the matrix, thus making it challenging to confirm the presence of these strengthening phases using XRD measurements. However, several other studies have demonstrated the presence of γ' and γ'' in the samples with the similar heat treatment procedure as this study using TEM [24, 26].

3.2.2 Microstructure of the FZ and HAZ

The microstructure of the FZ for all three welds is shown in Fig. 8. The presence of secondary phases can be seen in all of the welds. The secondary phases in the FZ of the welds are reported to be Laves and MC carbide phases in similar studies [27]. The precipitation of Laves phases in the FZ consumes the beneficial alloying elements such as Nb and Mo, which are crucial for strengthening phases to precipitate into the matrix, thus deteriorating the weld strength. It is reported that the brittle Laves and MC carbides phases could act as a suitable site for crack propagation in the FZ thus weakening the mechanical performance of the welds [28]. The Laves phases are distributed as long networked particles in the ABW (Fig. 8b) and WW (Fig. 8f), whereas the HTW displays a very discrete distribution of Laves phases in the FZ (Fig. 8d). The fraction area of the Laves phases is measured semi-quantitively using Image J, and the average values of five measurements is displayed in Fig. 9. It is noted that the ABW contains the highest volume fraction of Laves phases compared to the HTW and WW. This suggests that the heat treatment may help improve the weld strength by lowering the segregation of Nb into the FZ and decreasing the precipitation of harmful Laves phases. Similarly, other

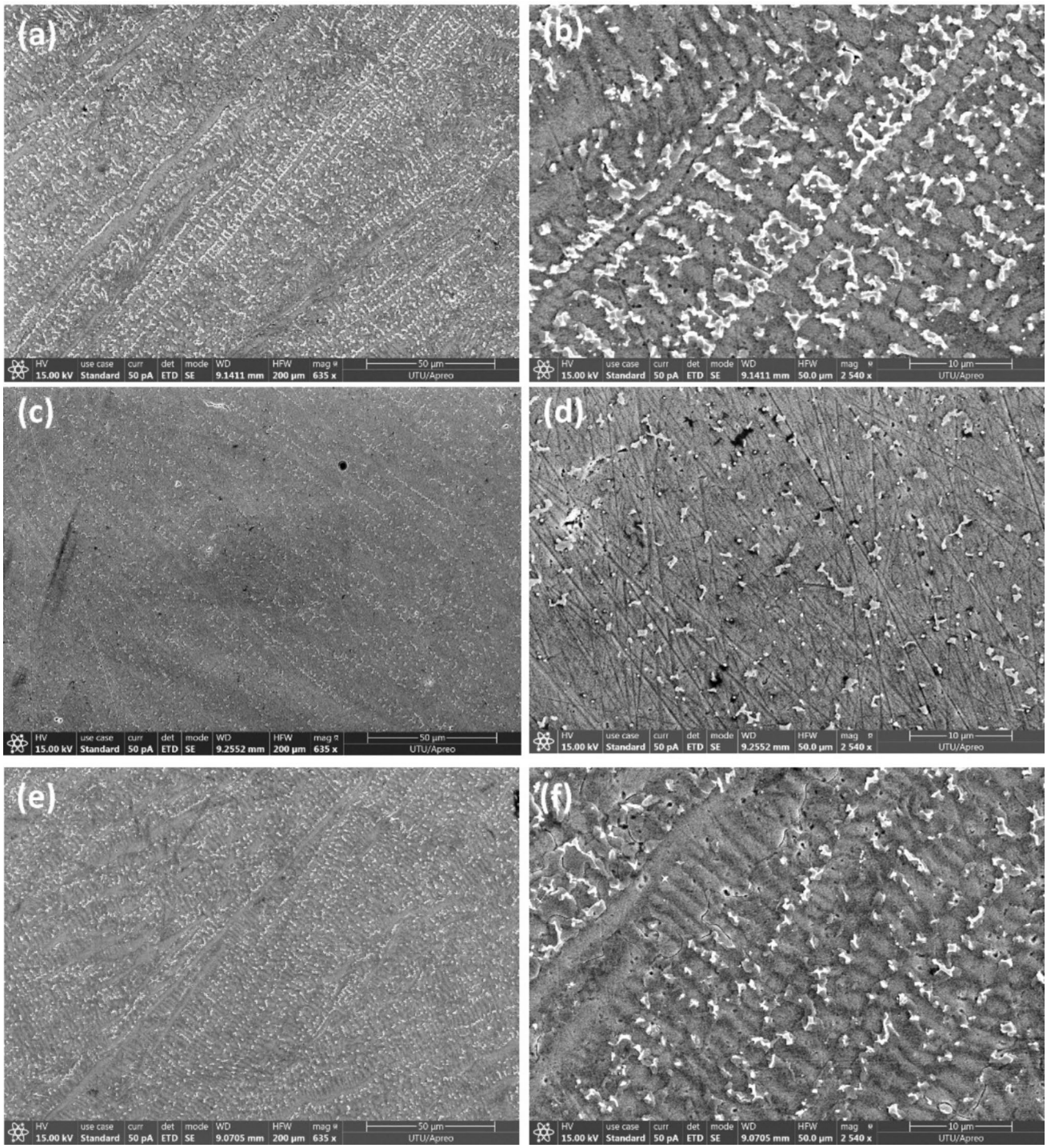

Fig. 8 Microstructure of the FZ in **a** ABW, **c** HTW, **e** WW. **b**, **d**, and **f** are the magnified images of **a**, **c**, and **e** respectively

studies also reported that pre-weld heat treatment could result in dissolution of the Laves phase in the base metal which improves the uniformity of Nb distribution in the Matrix [29, 30]. As a result, a more homogenized molten pool could reduce the segregation tendency of Nb and other alloying during solidification. Moreover, according to the discussion in Section 3.1, different thermophysical properties of the base metals could also impact the solidification rate during welding, therefore, changing the Laves phase distribution in the FZ.

The EDS mapping reveals the chemical composition of the secondary phases in the FZ as shown in Fig. 10. It is

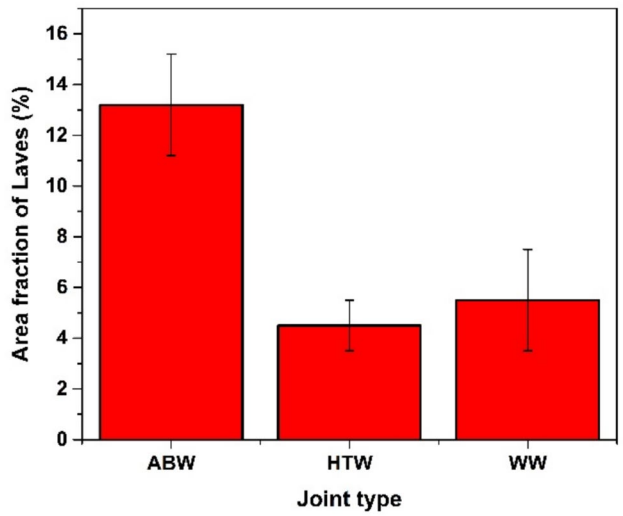

Fig. 9 Area fraction of Laves phases in the FZ of the welds

demonstrated that the secondary phases are rich in Nb and Ti as shown in Fig. 10e and g.

The point EDS analysis shows that these secondary phases contain almost four times higher Nb and Ti than the matrix as presented in Table 4. It should be noted that these values are not absolute as the EDS measurement is a semi-quantitative method and most likely the volume fraction of the interaction area is much larger than the segregations; thus, it is challenging to quantitively measure the chemical composition of each phases separately.

The XRD profile of the welds in the FZ is exhibited in Fig. 11. This confirms the presence of the Laves and MC carbides in the FZ of all three welds which is consistent with the microstructure images of the FZ (Fig. 8) and the EDS results.

The interface region between the FZ and HAZ is depicted in Fig. 12. All the welds demonstrate microfissures in the HAZ as illustrated by green circles in Fig. 12. Some discrete microcracks at the fusion line, as well as away from the fusion line, are observed in the WW (Fig. 12a), whereas the ABW and HTW indicate continuous cracks initiated from the fusion line and propagated towards the HAZ (Fig. 12b and d). The existence of distinct phases in the base metals may be the cause of the variations in the crack morphology. The BM consists of MC carbide phases, which resulted in liquation cracking at the grain boundaries in the HAZ during welding, while the BMHT and BMAB consist of Delta, Laves, and MC phases that are reported to be responsible for microfissuring in the HAZ [31]. This is consistent with the magnified image of the HAZ in the HT weld (Fig. 12d), where the presence of the Delta phase is observed; hence, it is worth noting that the precipitation of the Delta phase in the HAZ could be the reason for microfissuring in this type of weld. Note that the microcracks in the HAZ of the HTW seem to be backfilled (Fig. 12d). Other studies have suggested that segregation of elements such as S and B could be responsible for HAZ liquation cracking in Alloy 718 welds [32]. This needs further investigation to understand the root cause of HAZ liquation cracking in this type of joint, as well as how heat treatment could impact the HAZ cracking susceptibility.

3.3 Mechanical properties

3.3.1 Hardness test

The microhardness results of the welds are presented in Fig. 13. The average microhardness values of the welds in the FZ and base metals are summarized in Table 5. The BMHT shows an average microhardness of 510 HV, which is much higher than the average microhardness of the BM (230 HV) and BMAB (330 HV). This significant difference in hardness values of the base metals is caused by the two-stage solution and age hardening treatment that is done on the BMHT. The heat treatment is carried out to dissolve the Laves phases and precipitate hardening phases of γ' and γ'' into the matrix, which are responsible for such a high microhardness of the BMHT. However, the BM demonstrates the lowest average microhardness of 230 HV. This indicates that the annealing solution carried out on the wrought sample resulted in some softening and microstructure homogenization, which aligns with the BM microstructure characteristics (Fig. 6e).

The HTW highlights a significant drop in hardness compared to its base metal (BMHT). This could imply that the strengthening phases of γ' and γ'' are dissolved in the FZ of the HTW following the heating and cooling cycle of the laser welding process. Similarly, the ABW demonstrates a decrease in hardness values in the FZ compared to its base metal (BMAB). One major contributor to the hardness of the BMAB is the residual stress caused by the continuous heating and cooling cycles of the PBF-LB process. Therefore, this could indicate that laser welding could result in stress relieving of the ABW in the FZ, thus decreasing the hardness slightly compared to BMAB. In contrast, the WW shows an increase in hardness values in the FZ compared to its base metal (BM). This could be ascribed to the presence of hard and brittle Laves phases in the FZ of the WW [31]. The hardness results in the FZ supports the finding related to different Laves phase distribution in the FZs of the welds (Fig. 9) as the ABW shows the highest hardness compared to HTW and WW due to the denser distribution of the hard and brittle Laves phases in the FZ.

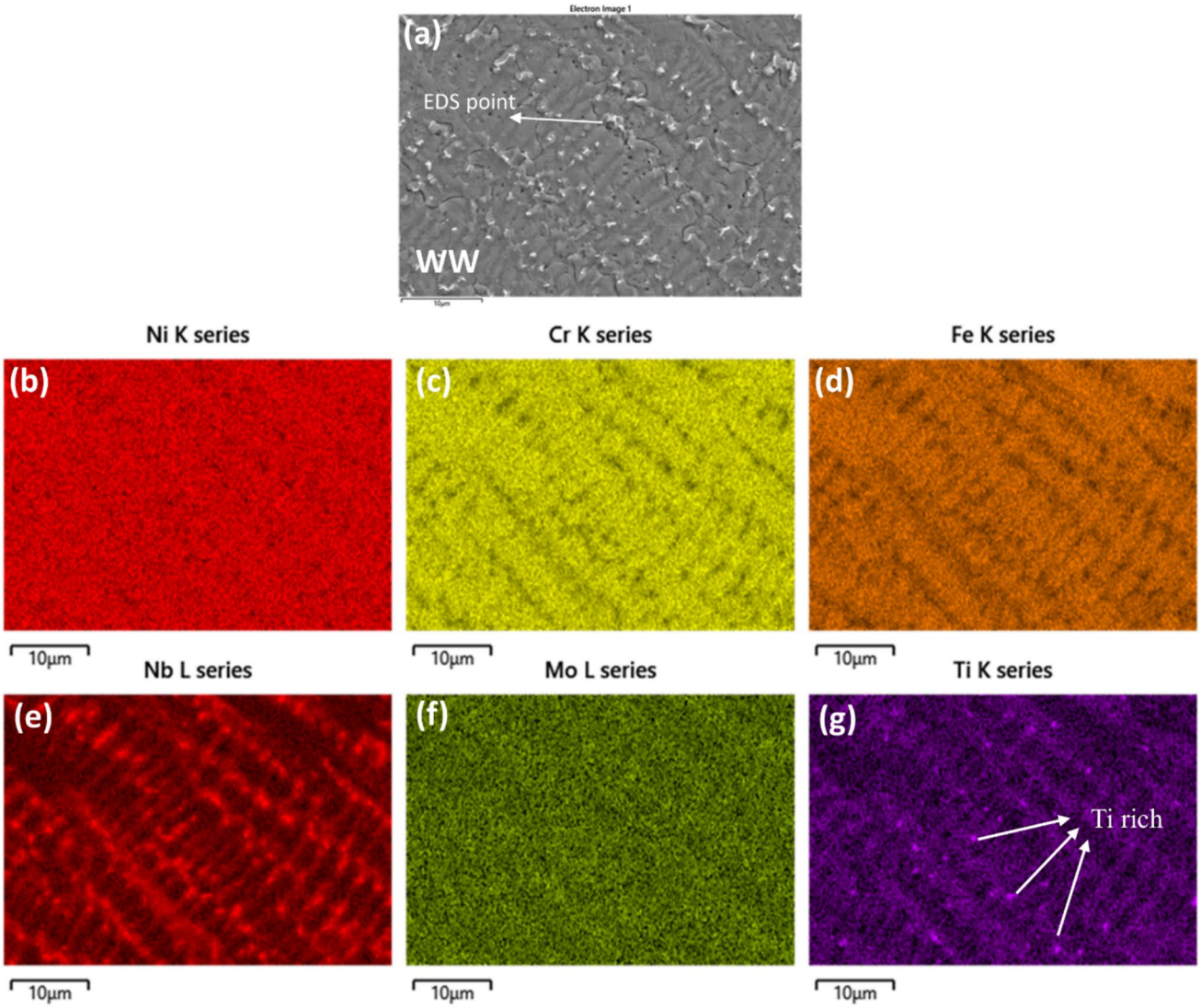

Fig. 10 EDS mapping analysis of **a** the FZ of WW showing the elemental distribution of **b** Ni, **c** Cr, **d** Fe, **e** Nb, **f** Mo, **g** and Ti

3.3.2 Tensile test

The tensile properties of the welds are presented in Fig. 14. The HTW demonstrates the highest ultimate tensile strength (UTS) and yield strength (YS) of 943 MPa and 720 MPa, respectively (Fig. 14a). The higher mechanical properties of the HTW could be correlated to the strengthening phases of γ′ and γ″ in the base metal, which act as a load-bearing region in this joint. However, the elongation is declined substantially (2% elongation) due to the softening in the FZ, which aligns with the results of the hardness measurement (Fig. 14b). The ABW exhibits a lower UTS and YT of 890 MPa and 560 MPa compared to the HTW; however, the elongation is improved noticeably to 24%. This indicates that the ABW could be a better choice for applications where ductility is a concern over the HTW; hence, the full heat treatment is not recommended in this regard, as it leads to brittle failure.

It should be noted that all the welds show comparable UTS and YS compared to the BM, as shown in Fig. 14a. This

Table 4 Chemical composition of the point EDS analysis in Fig. 10a

Elements	Ni	Cr	Fe	Nb	Mo	Ti	Al
EDS point	44.7	16.2	14.7	16.8	2.5	4.7	0.4

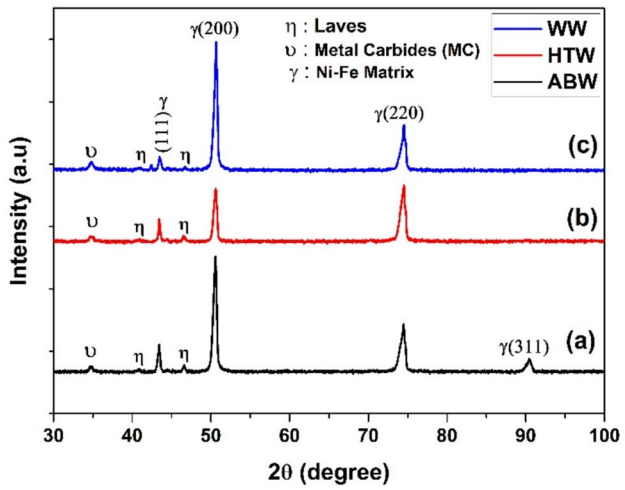

Fig. 11 XRD profile of the welds in the FZ of **a** ABW, **b** HTW, **c** WW

indicates that a high-quality weld can be achieved for PBF-LB/IN718 and wrought Alloy 718 parts using laser welding. Nevertheless, the ductility is declined in all the welds compared to the BM as seen in Fig. 14b. The decline in ductility could be attributed to two factors, one is the presence of brittle Laves phases in the FZ [11], and the other one is the pore formation during laser welding of Alloy 718 [33, 34].

Some pores with dimensions of 20–200 µm were observed in the FZ in all of the welds as shown in Fig. 15. The low fluidity of Ni alloys and the rapid solidification rate of the laser welding process are the root causes of the pore formation in laser keyhole welding of Alloy 718, resulting in too short of a time for gas bubbles to escape from the molten pool, thus forming pores [35]. The trapped gas in the molten pool could be either generated by the contamination on the weld joint surface or from the interaction of the shielding gas with the molten pool. The interaction of the shielding gas or contaminant with the molten pool results in instability of

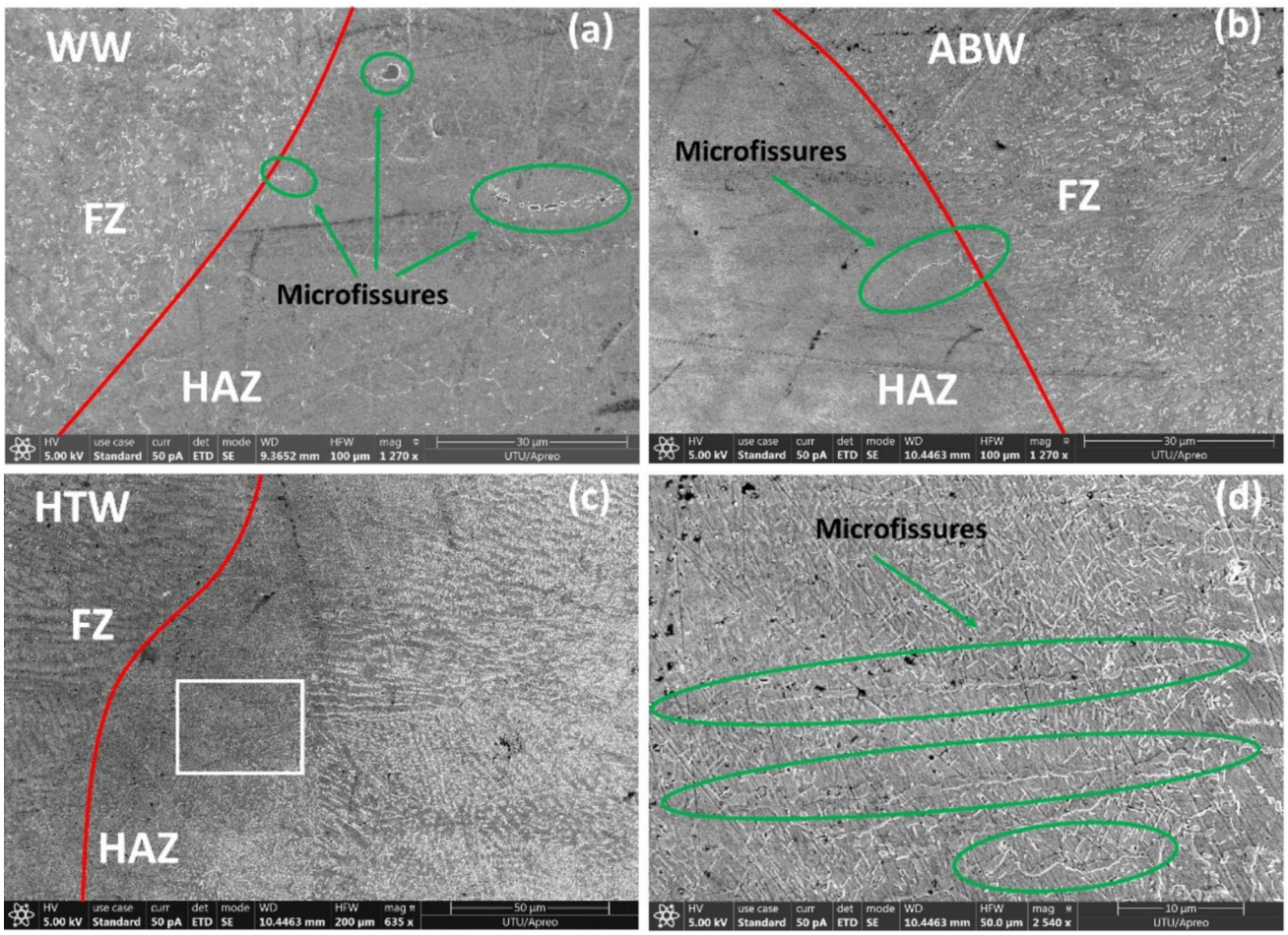

Fig. 12 Microfissures in the interface region between FZ and HAZ in **a** WW, **b** ABW, **c** HTT. **d** Magnified image of the rectangle region in **c**

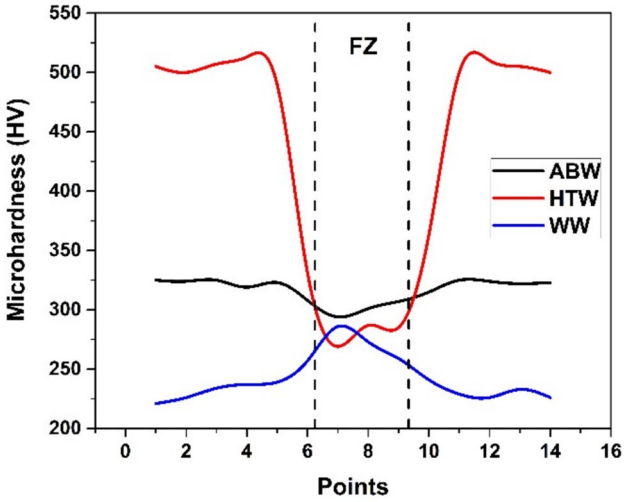

Fig. 13 Hardness values of the welds

Table 5 Average microhardness values of the welds in the FZ

Microhardness values	AB	HT	AW
FZ	297 ± 3	280 ± 8	279 ± 6
Base metals	340 ± 7	480 ± 6	230

the keyhole, which leads to gas bubbles being trapped in the molten pool. In another study, laser welding parameters, particularly laser power, are reported to play a role in eliminating the trapped gas bubbles [33]. The samples in this study were cleaned before welding, and heat treatment was also performed under controlled Ar gas flow; thus, the impact of the contaminant on the surface might be minor in this study. However, it has been reported that employing a shielding gas other than Ar helps to reduce porosity in laser welding of Alloy 718 [35]. Thus, this needs further investigation to fully understand which factors are contributing greatly to pore formation in laser keyhole welding of Ni-based alloys.

The fracture analysis of the welds revealed that the HTW failed completely at the FZ, whereas the WW and ABW showed fracture occurring at the fusion line and deflecting to the FZ, as schematically depicted in Fig. 16. This would suggest that the fusion line of these welds was the weak point because of the microfissuring, and that the fracture was diverted into the FZ by the presence of Laves phases and porosities in the FZ. Consequently, porosities, brittle Laves phases, and microfissures all have a significant impact on the mechanical characteristics of these types of welds.

The fracture surface of the welds in the FZ is depicted in Fig. 17. It can be seen that all of the welds show similar fracture surface with the ABW and WW exhibiting higher fraction of secondary Laves phases (brighter regions) in the FZ which aligns with the results of the microstructure analysis of the welds (Fig. 9). The dimples on the fracture surface of the welds indicates a ductile failure mechanism in all the welds, and secondary cracks (due to the presence of Laves phases) is observed in the ABW (Fig. 17a).

3.3.3 Fatigue test

The fatigue strength of the welds at 10^6 cycles is displayed in Fig. 18. The results of the fatigue tests are summarised in Table 6. The WW demonstrate superior fatigue strength (151 MPa) compare to the HTW (120 MPa) and ABW (114 MPa). In a survey study by [36], the average fatigue limit of PBF-LB/IN718 at

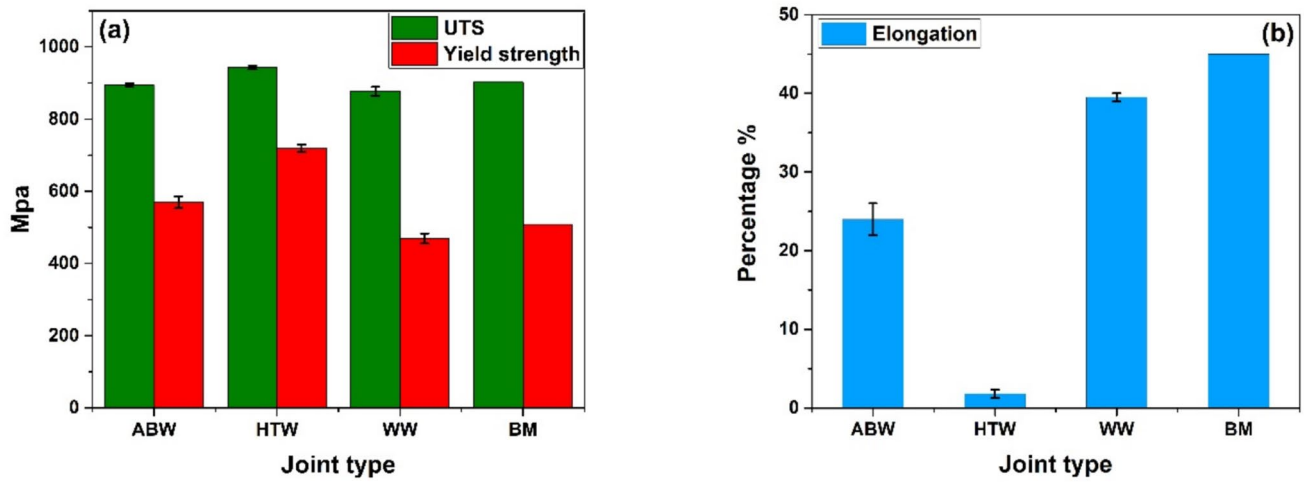

Fig. 14 **a** Ultimate tensile strength and yield strength of the welds, **b** elongation at break of the welds

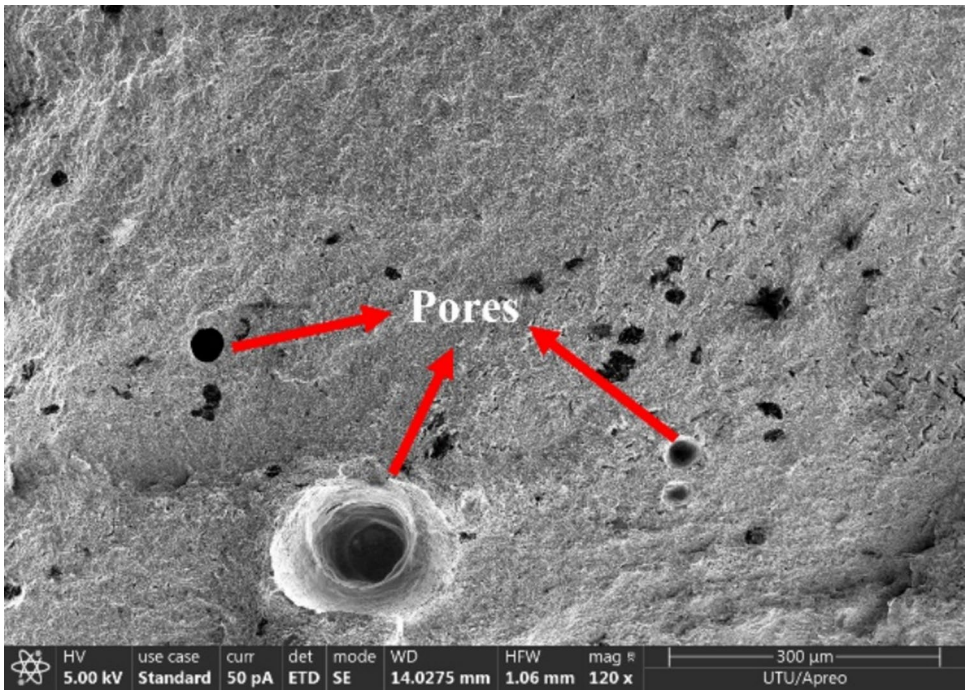

Fig. 15 Pores in the FZ of ABW

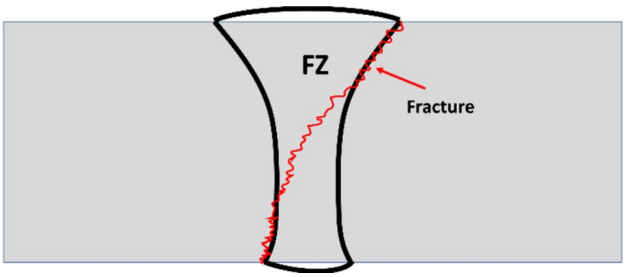

Fig. 16 Schematic of fracture path in the WW and ABW

R = 0.1 is predicted to be around 145 MPa; however, our results show somewhat more conservative results of 120 MPa. This is mainly due to the scattered fatigue data and also the fact that we had only limited number of samples for these tests. In addition, surface quality of the fatigue test samples, building direction, manufacturer, and parameters used for printing are important factors that influence the fatigue results.

The differences in the fatigue strength of the welds is explained by the fracture surface analysis as shown in Fig. 18. It is observed that the ABW and HTW fractured in the base metals far from the FZ due to the lack of fusion on the surface of the samples, while the WW fractured in the FZ due to porosity and undercut. Therefore, it can be concluded that the manufacturing defects such as lack of fusion in the PBF-LB samples are more detrimental to the fatigue life than the weld geometry defects such as undercut and porosity.

Furthermore, the fracture surface of the ABW shows a brittle intergranular cleavage (Fig. 19a) on the surface with

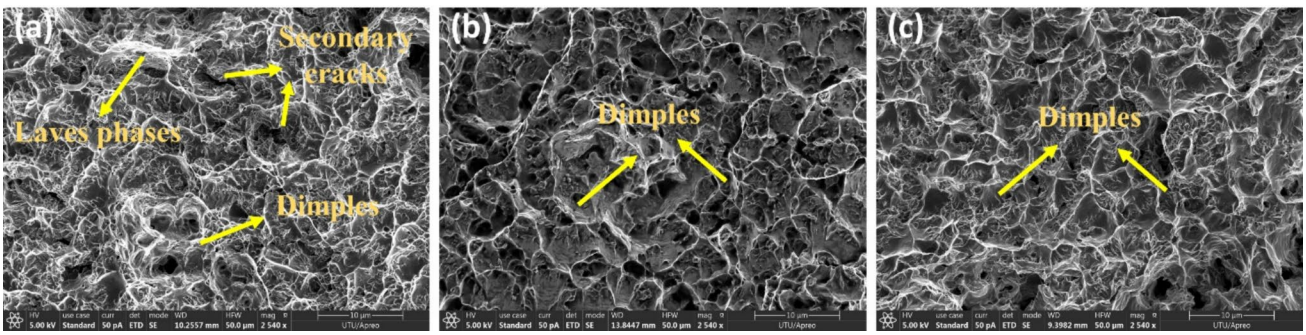

Fig. 17 Tensile fracture surface of **a** ABW, **b** HTW, **c** WW

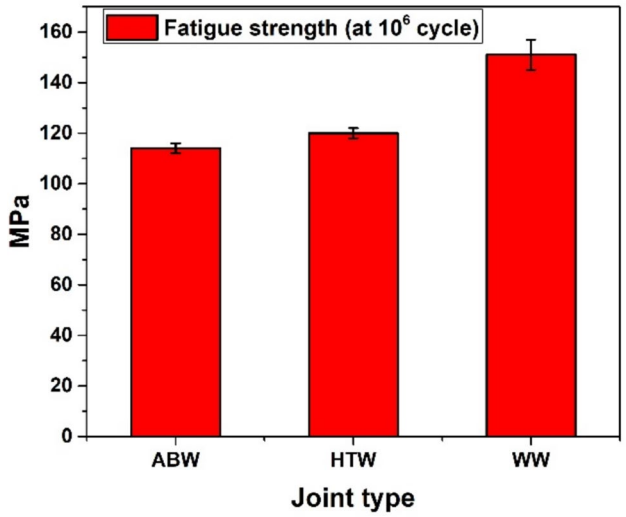

Fig. 18 Fatigue strength of the welds at 16^5 cycles

striations (Fig. 19b) resulting from the cyclic loading. During the cyclic loading, the cracks initiated on the surface due to the lack of fusion defects and propagated through the BMAB in a brittle manner [37]. Moreover, the presence of brittle Laves phases in the BMAB could also impact the fatigue strength, as some secondary cracks are observed on the fracture surface. The HTW exhibits dimples on the fracture surface at much higher magnification (Fig. 19d), indicating a ductile failure mechanism and slight improvement in the fatigue strength. The stress relieving following the heat treatment and dissolution of the Laves phase could be attributed to the slightly higher fatigue strength of the HTW compared to the ABW [33]. It should be noted that the fracture surface of the HTW exhibits some secondary cracks despite the dissolution of Laves phases. This could be ascribed to the presence of delta phases, which could impact the fatigue properties of this type of weld [38]. Finally, the fracture surface of the WW reveals ductile failure mechanics due to the presence of dimples on the surface, resulting in the highest fatigue strength (Fig. 19e and f).

4 Conclusion

This study investigated the weldability of PBF-LB/IN718 using laser welding. The microstructure and mechanical properties of the welds were compared with wrought Alloy 718. In addition, the influence of pre-weld heat treatment on the mechanical and microstructure of the welds was evaluated. The summary of the results can be outlined as follows:

- The BMAB and BMHT exhibited secondary phases of Laves, MC carbides, and delta phases, whereas the base metal of wrought Alloy 718 (BM sample) showed small traces of MC carbides. It was determined that distinct secondary phase precipitation in the samples was caused by various heat treatment procedures.
- All of the welds displayed Nb and Ti rich segregation in the FZ, which was identified as Laves and MC carbides. The Laves phase was distributed more densely in the ABW as a long-networked particle, while the HTW and WW showed a very discrete distribution of the Laves phases in smaller volumes.
- The mechanical properties of the welds, such as UTS and YS in all the welds, were comparable to the BM, indicating a high-strength weld was achieved using laser welding. However, the ductility of the welds was inferior to that of the BM due to the presence of brittle Laves phase and porosity in the FZ and HAZ microfissuring.
- The fatigue strength of the ABW and HTW was inferior to that of the WW. The manufacturing defect, such as lack of fusion and porosities in the BMAB and BMHT, was identified as the reason for their inferior fatigue strength.

Table 6 Fatigue test results of the welds (three tests per each weld)

Joint type	Stress amplitude at failure (MPa)	Number of steps	Number of cycles at failure n ($\times 10^5$)	Estimated fatigue strength (MPa)	Average of fatigue strengths (MPa)
ABW	120	2	2.8	113	115
	120	2	3.2	114	
	120	2	5.1	116	
HTW	120	2	7.9	120	120
	120	2	6.5	118	
	120	2	9.0	121	
WW	160	3	1.1	152	151
	160	3	0.8	150	
	160	3	1.5	153	

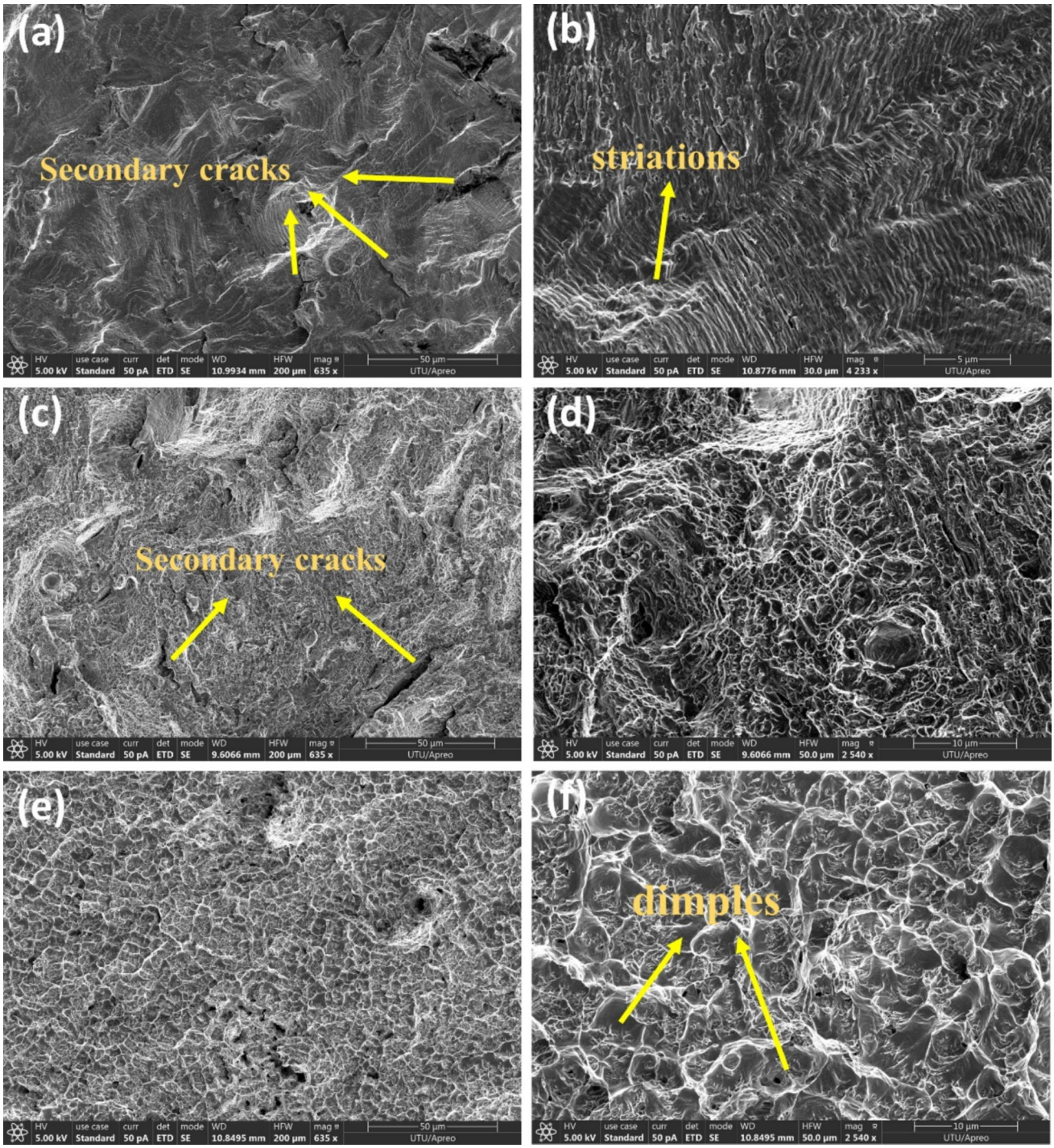

Fig. 19 Fatigue fracture surface of **a** and **b** ABW, **c** and **d** HTW, **e** and **f** WW

Acknowledgements The authors would like to thank Dr.Abdul-Shaafi. Shaikh from EOS Finland Oy for manufacturing the PBF-LB/IN718 samples. The author would like to acknowledge LUT University for preparing the samples for SEM analysis and University of Oulu for conducting the tensile and fatigue tests. The authors also acknowledge the Materials Research Infrastructure (MARI) at the Department of Physics and Astronomy, University of Turku for access and support with the SEM and XRD facilities.

Author contribution Saeid Parchegani Chozaki: writing—review and editing, writing—original draft, investigation, formal analysis, data curation, conceptualization; Heidi Piili: supervision, review and

editing; Olli Nyrhila: resources; Antti Salminen: review and editing, funding acquisition, supervision.

Funding Open Access funding provided by University of Turku (including Turku University Central Hospital). This work was financed by the projects CaNeLis funded by business Finland and VADILA project funded by European Regional Development Fund.

Data availability The data that support the findings of this study are available upon reasonable request.

Declarations

Competing interest The authors declare no competing interests.

References

1. Mostafaei A, Ghiaasiaan R, Ho IT, Strayer S, Chang KC, Shamsaei N, Shao S, Paul S, Yeh AC, Tin S, To AC (2023) Additive manufacturing of nickel-based superalloys: a state-of-the-art review on process-structure-defect-property relationship. Prog Mater Sci 136:101108
2. Kracke A (2013) Superalloys, the most successful alloy system of modern times-past, present, and future. In: Proceedings of the 7th International Symposium on Superalloy 718 and Derivatives, Pittsburgh
3. Mahesh K, Philip JT, Joshi SN, Kuriachen B (2021) Machinability of Inconel 718: a critical review on the impact of cutting temperatures. Mater Manuf Process 36(7):753–791
4. Attaran M (2017) The rise of 3-D printing: the advantages of additive manufacturing over traditional manufacturing. Bus Horiz 60:677e88
5. Herzog D, Seyda V, Wycisk E, Emmelmann C (2016) Additive manufacturing of metals. Acta Mater 117:371–392
6. Zhang B, Li Y, Bai Q (2017) Defect formation mechanisms in selective laser melting: a review. Chin J Mech Eng 30:515–527
7. Gong H (2013) Generation and detection of defects in metallic parts fabricated by selective laser melting and electron beam melting and their effects on mechanical properties. Dissertation, Doctor of Philosophy, Department of Industrial Engineering, University of Louisville, Louisville
8. Parchegani S, Piili H, Ganvir A, Salminen A (2023) Laser welding of additively manufacture parts- A Review. IOP Conf Ser: Mater Sci Eng 1296:012030. https://doi.org/10.1088/1757-899X/1296/1/012030
9. Hebert RJ (2016) Viewpoint: metallurgical aspects of powder bed metal additive manufacturing. J Mater Sci 51:1165–1175
10. Sonar T, Balasubramanian V, Malarvizhi S, Venkateswaran T, Sivakumar D (2021) An overview on welding of Inconel 718 alloy - effect of welding processes on microstructural evolution and mechanical properties of joints. Mater Charact 174:110997
11. Sivaprasad K, Ganesh Sundara Raman S (2008) Influence of weld cooling rate on microstructure and mechanical properties of Alloy 718 weldments. Metall Mater Trans A 39:2115–2127
12. Qian M, Lippold JC (2003) Liquation phenomena in the simulated heat-affected zone of alloy 718 after multiple post weld heat treatment cycles. Weld J 82(6):145S-150S
13. Janaki Ram GD, Venugopal Reddy A, Prasad Rao K, Madhusudhan Reddy G (2004) Control of laves phase in Inconel 718 GTA welds with current pulsing. Sci Technol Weld Join 9(5):390–398
14. Sonar T, Balasubramanian V, Malarvizhi S (2020) Effect of heat input on evolution of microstructure and tensile properties of gas tungsten constricted arc (GTCA) welded Inconel 718 alloy sheets. Metallogr Microstruct Anal 9:369–392
15. Manikandan S, Sivakumar D, Rao KP et al (2016) Effect of enhanced cooling on microstructure evolution of alloy 718 using the gas tungsten arc welding process. Weld World 60:899–914
16. Odabaşı A, Ünlü N, Göller G (2010) A study on laser beam welding (LBW) technique: effect of heat input on the microstructural evolution of superalloy Inconel 718. Metall Mater Trans A 41:2357–2365
17. Chozaki SP, Piili H, Afkhami S et al (2025) Investigation of the microstructure and mechanical properties of dissimilar joints of PBF-LB/IN718 to AISI 316L by laser welding. Weld World 69:1829–1845
18. Jokisch T, Marko A, Gook S, Üstündag O, Gumenyuk A, Rethmeier M (2019) Laser welding of SLM-manufactured tubes made of IN625 and IN718. Materials 12:2967
19. Simón-Muzása J, Brunner-Schwerb C, Hilgenberga K, Rethmeierc M (2023) Mechanical properties of laser welded joints of wrought and heat-treated PBF-LB/M Inconel 718 parts depending on build direction, Lasers in Manufacturing Conference, LiM 2023, ICM - International Congress Center, Munich. https://doi.org/10.24406/publica-1965
20. Maxwell DC, Nicholas T (1999) A rapid method for generation of a Haigh diagram for high cycle fatigue. In: Fatigue and Fracture Mechanics: 29th Volume. ASTM International
21. Abroug F, Monnier A, Arnaud L, Balcaen Y, Dalverny O (2022) High cycle fatigue strength of additively manufactured AISI 316L Stainless Steel parts joined by laser welding. Eng Fract Mech 275:108865
22. Mokhtari M, Pommier P, Balcaen Y, Alexis J (2021) Laser welding of AISI 316L stainless steel produced by additive manufacturing or by conventional processes. J Manuf Mater Process 5:136
23 Matilainen V, Pekkarinen J, Salminen A (2016) Weldability of additive, manufactured stainless steel. Phys Procedia 83:808–817
24. Deng D, Peng RL, Brodin H, Moverare J (2018) Microstructure and mechanical properties of Inconel 718 produced by selective laser melting: sample orientation dependence and effects of post heat treatments. Mater Sci Eng A 713:294–306
25. Yang H, Wang Z, Wang H, Wu Y, Wang H (2023) Microstructure, mechanical property and heat treatment schedule of the Inconel 718 manufactured by low and high-power laser powder bed fusion. Mater Sci Eng A 863:144517
26. Hamada A, Ghosh S, Rautio T et al (2025) Strengthening and embrittlement mechanisms in laser-welded additively manufactured Inconel 718 superalloy. Weld World 69:81–98. https://doi.org/10.1007/s40194-024-01897-0
27. Radhakrishna CH, Prasad Rao K (1997) The formation and control of Laves phase in superalloy 718 welds. J Mater Sci 32:1977–1984. https://doi.org/10.1023/A:1018541915113
28. Patil S, Jha A, Sankar Ganesh P, Petley V, Rajeswari S, Shariff SM, Ramji M, Muvvala G (2025) A study on laser welding of Inconel 718 and evolution of strain field using digital image

correlation to estimate the localized properties. Opt Laser Technol 184:112472
29. Zhao L, Tan Y, Wang Y, You X, Chang K, Zhuang X, Li P, Hu Y (2021) Homogenization behavior of IN 718 superalloy prepared by electron beam layered solidification technology. J Mater Res Technol 13:1567–1575
30. Fayed EM, Shahriari D, Saadati M, Brailovski V, Jahazi M, Medraj M (2020) Influence of homogenization and solution treatments time on the microstructure and hardness of Inconel 718 fabricated by laser powder bed fusion process. Materials 13(11):2574
31. Cao X, Rivaux B, Jahazi M, Cuddy J, Birur A (2009) Effect of pre- and post-weld heat treatment on metallurgical and tensile properties of Inconel 718 alloy butt joints welded using 4 kW Nd:YAG laser. J Mater Sci 44:4557–4571
32. Chaturvedi MC (2007) Liquation cracking in heat affected zone in Ni superalloy welds. MSF 546:1163–1170. https://doi.org/10.4028/www.scientific.net/msf.546-549.1163
33. Kuo T-Y (2005) Effects of pulsed and continuous Nd–YAG laser beam waves on welding of Inconel alloy. Sci Technol Weld Joi 10(5):557–565. https://doi.org/10.1179/174329305X46709
34 Adomako NK, Park HC, Cha SC, Lee M, Kim JH (2021) Microstructure evolution and mechanical properties of the dissimilar joint between IN718 and STS304. Mater Sci Eng A 799:140262
35. Elmer JW, Vaja J, Pong R, Gooch TH, Barth HD (2015) The effect of Ar and N2 shielding gas on laser weld porosity in steel, stainless steel, and nickel. United States. https://www.osti.gov/servlets/purl/1812143
36. Mills M, Thomas M (2024) A survey of the high-cycle fatigue performance of additively manufactured alloy 718. Mater Sci Technol 40(17):1235–1244
37. Zhong L, Hu H, Liang Y, Huang C (2019) High cycle fatigue performance of Inconel 718 alloys with different strengths at room temperature. Metals 9:13. https://doi.org/10.3390/met9010013
38. Juraj B, Vaško A, Kuchariková L, Tillová E, Matvija M (2018) The high-temperature loading influence on orthorhombic Ni3Nb DOa δ-phase formation and its effect on fatigue lifetime in alloy 718. Manuf Technol 18(6):875–882